

Application of a model of internal hydraulic jumps

Thorpe, Stephen; Malarkey, Jonathan; Voet, Gunnar; Alford, Mathew; Girton, James; Carter, Glenn

Journal of Fluid Mechanics

DOI:

[10.1017/jfm.2017.646](https://doi.org/10.1017/jfm.2017.646)

Published: 10/01/2018

Peer reviewed version

[Cyswllt i'r cyhoeddiad / Link to publication](#)

Dyfyniad o'r fersiwn a gyhoeddwyd / Citation for published version (APA):

Thorpe, S., Malarkey, J., Voet, G., Alford, M., Girton, J., & Carter, G. (2018). Application of a model of internal hydraulic jumps. *Journal of Fluid Mechanics*, 834, 125-148.
<https://doi.org/10.1017/jfm.2017.646>

Hawliau Cyffredinol / General rights

Copyright and moral rights for the publications made accessible in the public portal are retained by the authors and/or other copyright owners and it is a condition of accessing publications that users recognise and abide by the legal requirements associated with these rights.

- Users may download and print one copy of any publication from the public portal for the purpose of private study or research.
- You may not further distribute the material or use it for any profit-making activity or commercial gain
- You may freely distribute the URL identifying the publication in the public portal ?

Take down policy

If you believe that this document breaches copyright please contact us providing details, and we will remove access to the work immediately and investigate your claim.

Application of a model of internal hydraulic jumps

Journal:	<i>Journal of Fluid Mechanics</i>
Manuscript ID	JFM-17-S-0400.R1
mss type:	Standard
Date Submitted by the Author:	28-Jul-2017
Complete List of Authors:	Thorpe, S. A.; U. of Bangor, UK, School of Ocean Sciences; Malarkey, Jonathan; Bangor University Voet, Gunnar; University of Southern California Alford, Matthew; University of Southern California Girton, James; University of Washington, Applied Physics Laboratory; Carter, Glenn; University of Hawaii at Manoa, Department of Oceanography
Keyword:	Hydraulic control < Geophysical and Geological Flows, Stratified flows < Geophysical and Geological Flows, Turbulent transition < Turbulent Flows

Application of a model of internal hydraulic jumps

S.A.Thorpe¹*, J.Malarkey¹, G.Voet², M.H.Alford², J.B.Girton³ and G.S.Carter⁴

¹ School of Ocean Sciences, Bangor University, Menai Bridge, Anglesey LL59 5AB, UK

² Scripps Institution of Oceanography, University of California, San Diego, CA 92093, USA

³ Applied Physics Laboratory, University of Washington, Seattle, WA 98105, USA

⁴ Department of Oceanography, University of Hawaii, Honolulu, HI, 96822, USA

Submitted 25th March 2017; editor's reply 8th June 2017; revised & resubmitted 28th July 2017

A model devised by Thorpe & Li (2014, *J. Fluid Mech.* **758**, 94-120) that predicts the conditions in which stationary turbulent hydraulic jumps can occur in the flow of a continuously stratified layer over a horizontal rigid bottom is applied to, and its results compared with, observations made at several locations in the ocean. The model identifies two positions in the Samoan Passage at which hydraulic jumps should occur and where changes in the structure of the flow are indeed observed. The model predicts the amplitude of changes and the observed mode 2 form of the transitions. The predicted dissipation of turbulent kinetic energy is also consistent with observations. One location provides a particularly well-defined example of a persistent hydraulic jump. It takes the form of a 390 m thick and 3.7 km long mixing layer with frequent density inversions separated from the seabed by some 200 m of relatively rapidly moving dense water, thus revealing the previously unknown structure of an internal hydraulic jump in the deep ocean. Predictions in the Red Sea Outflow in the Gulf of Aden are relatively uncertain. Available data, and the model predictions, do not provide strong support for the existence of hydraulic jumps. In the Mediterranean Outflow, however, both model and data indicate the presence of a hydraulic jump.

1. Introduction

Little is known of the form and structure of hydraulic jumps in the deep ocean, and until recently measurements in and around features that satisfy the dynamical conditions necessary for hydraulic transitions to occur have been lacking. The potential importance of hydraulic jumps as a mechanism for mixing in stratified near-bed currents is however recognised and several studies have been made of the flow in regions where jumps might be expected, notably in the Romanche Fracture Zone (Polzin et al., 1996) and in the near-bottom outflows from both the Red Sea (Peters & Johns, 2005; Peters et al., 2005) and from the Mediterranean Sea (Gasser et al., 2011; Nash et al., 2012). Alford et al. (2013) conclude that hydraulic jumps form downstream of a sill in the Samoan Passage, resulting in turbulent mixing. In the atmosphere transitions in pressure, wind speed and potential temperature described as being caused by hydraulic jumps have been observed, for example, in the lee of the Sierra Nevada mountain range in California by Armi & Mayr (2011) and in katabatic winds in Adélie Land in Antarctica by Pettré & André (1991), the latter a manifestation of “Loewe’s phenomenon” (Baines, 1995).

*Email address for correspondence: s.a.thorpe@bangor.ac.uk

Our purpose here is to apply an idealized model in some of these regions where detailed measurements of near bottom flows are available and jumps appear likely. The theoretical model predicts when flows are prone to hydraulic jumps and, if they are, the amplitude of jumps and what loss of energy occurs. The comparison with observations provides tests of the validity of the model and, within the limits of the model and its ‘fit’ to the data, examination of whether hydraulic jumps occur in observed flows and some indication of their nature.

The model is described in § 2, and applied to data in the following sections. § 3 makes comparison with observations over and in the lee of a sill in the Samoan Passage. Two abrupt changes in the character of the flow are examined in detail and are identified as hydraulic jumps. In § 4 the model predictions are applied to observations in the Red Sea Outflow, whilst § 5 describes comparison of the model with observations in the Mediterranean Outflow. The main conclusions are discussed in § 6 and summarized in § 7.

2. The model

A theoretical model of a stationary turbulent internal hydraulic jump in a non-rotating system is devised by Thorpe & Li (2014) (hereafter referred to as TL) and illustrated in figure 1. A stratified layer in which the jump occurs flows over a rigid horizontal boundary at $z = 0$ and beneath a uniform stationary fluid of infinite depth. Unlike the majority of models of such jumps which assume that the flow consists of two discrete uniform layers upstream of the hydraulic transition (reviewed, for example, by Ogden & Helfrich, 2016, and Baines, 2016), TL adopt continuous profiles of velocity and density both upstream and downstream of the transition. The velocities in the model are given by

$$u_i(z) = U_i F_i(z/h_i), \quad (1)$$

where subscript $i = 1$ indicates a steady flow approaching a jump (‘upstream’) and $i = 2$ indicates a steady flow beyond the jump (‘downstream’) when turbulence generated within the region of the transition has collapsed, and h_i is the thickness of the flowing layers. The (positive) functions F_i are selected as ‘ η profiles’; for a given value, η_i , and with $y = z/h_i$:

$$\begin{aligned} F_i(y) &= 1, & \text{if } 0 \leq y \leq \eta_i \leq 1 \text{ (a uniform lower layer),} & \uparrow \\ &= (1-y)/(1-\eta_i), & \text{if } \eta_i \leq y \leq 1 \text{ (an interfacial layer),} & \} (2) \\ &= 0, & \text{if } y \geq 1 \text{ (a uniform and stationary upper layer).} & \downarrow \end{aligned}$$

The η profiles provide examples of flows ranging from a uniform gradient extending from $z = 0$ to $z = h_i$ when $\eta_i = 0$ to a two-layer structure with discontinuity at $z = h_i$ when $\eta_i = 1$.

The density is chosen with a profile similar to the velocity:

$$\rho_i(z) = \rho_0[1 - \Delta + 2\Delta F_i(z/h_i)]. \quad (3)$$

The reference density, ρ_0 , and the measure of density variation, Δ (and the velocity measures, U_i), are all positive. The density at the boundary, $z = 0$, is $\rho_0(1 + \Delta)$ in the upstream flow and also in the downstream flow. (This requirement of equal densities

at $z = 0$ can be relaxed to allow mixing in the transition to extend through the lower layer down to the seabed, so reducing the density in the downstream flow at $z = 0$ and introducing a measure, δ , of the density change, as described by Thorpe, 2010, and TL.) The density gradients, $d\rho/dz$, are zero except in the interfacial layer where they equal $-2\Delta\rho_0/[h_i(1 - \eta_i)]$. Above $z = h_i$ the density is equal to $\rho_0(1 - \Delta)$ and, since the density is uniform, no internal waves can propagate upwards from the transition region (but see appendix C later). It is assumed that the transition is not undular; no allowance is made for mixing and energy loss in a train of stationary waves downstream of a jump. The downstream profiles defined by U_2 , h_2 and η_2 depend on the turbulent mixing in the jump but are made to be consistent with their upstream values, U_1 , h_1 and η_1 , according to the laws of conservation of volume, mass and momentum fluxes.

The η profiles at locations upstream and downstream of perceived hydraulic jumps are fitted to the data as explained in appendix A to obtain values of η_i , U_i , h_i and $2\Delta\rho_0$. The gradient Richardson number in the interfacial layer ($\eta_i h_i < z < h_i$) is

$$Ri_i = 2g\Delta h_i(1 - \eta_i)/U_i^2. \quad (4)$$

Closure is obtained by assuming that the downstream interfacial Richardson number, Ri_2 , equals $1/3$. This value is chosen because by the Miles-Howard theorem it ensures that the downstream flow is stable. Furthermore it is well within the bounds of uncertainty of the final values, Ri_F , of Richardson numbers in laboratory and numerical studies of decaying turbulence following Kelvin Helmholtz instability (KHI) in a stratified interfacial layer (e.g., Thorpe, 1973; Smyth, Moum & Caldwell, 2001. It should however be noted that whether there is a similar limiting Richardson number following the collapse of turbulence initiated in a hydraulic jump is not known, although a value of about $1/3$ is indeed found downstream of the jumps analysed in § 3.) The upstream flow is characterised by η_1 and a Froude number, Fr , defined as

$$Fr = U_1^2/(g\Delta h_1) = 2(1 - \eta_1)/Ri_1. \quad (5)$$

Figure 2 summarizes the analysis of three factors important in internal hydraulic jumps: wave propagation, consistency with the conservation laws, and the stability of the upstream and downstream flows; it shows the character of flows satisfying the conservation laws and the possibility of transitions at points in the (η_1, Fr) plane defining the upstream flow. A necessary condition for a steady stationary jump is that no waves can propagate upstream to alter the flow in which the jump occurs. The bold lines of figures 2a and 2b are derived by Thorpe (2010; see his § 4.2) and indicate limiting values for this condition to apply. They mark the maximum value of Fr for given η_1 at which waves can propagate in the upstream direction; at greater values of Fr (when jumps can be stationary) there are no upstream travelling waves. When $\eta_1 < 2/3$, the limiting Froude number equals $8(1 - \eta_1)$ and (5) implies that $Ri_1 = 1/4$. (The condition $Ri_1 = 1/4$ is satisfied on the dashed line and on its continuation to $Fr = 8$ at $\eta_1 = 0$ in figures 2a and 2b.) Figure 2b, found following TL, also shows where finite amplitude jumps consistent with the conservation laws may be possible in given upstream flows, i.e. at points in the (η_1, Fr) plane. To the right of the bold line marking the limiting Fr the plane is divided into three regions, A, B and C. No jumps are possible in region A. Just one solution of the conservation equations for a flow

downstream of a jump is possible in region C (meaning that only one type of jump or mode of transition can occur). Two solutions exist in region B; one of two jumps are possible but only when η_1 exceeds 0.74 and Fr is sufficiently large. Jumps occur in the regions B and C where the upstream flow with corresponding η_1 and Fr is described as ‘supercritical’ to the formation of hydraulic jumps. Jumps are not supported in the remaining regions of the (Fr, η_1) plane; these flows are ‘subcritical’. The smallest Fr at which a jump can occur is 2.2 when $\eta_1 = 0.74$, at the junction of regions B and C and the bold line. The single roots in region C generally correspond to mode 2 jumps (figure 1b) in which the interfacial layer in the upstream flow, $\eta_1 h_1 < z < h_1$, expands both upwards and downwards; values of h_2 exceed h_1 but $\eta_1 h_1 > \eta_2 h_2$, so that the upper isopycnals rise and the lower descend. The double roots of region B are either of mode 2 jumps or those of mode 1, in which all isopycnals rise through the transition as illustrated in figure 1a.

The stability of the upstream flow is examined by TL (their § 2.2) and summarized in figure 2c. The hatched region shows where KHI is not possible in the upstream flow, i.e., where the Taylor-Goldstein equation describing the stability of small perturbations to the flow has no exponentially growing solutions. KHI may occur in the remaining region of the (η_1, Fr) plane. A value $Ri_1 = 1/3$ corresponds to the dot-dash line, $Fr = 6(1-\eta_1)$. Points on this line are to the left of, and outside, the supercritical regions B and C of figure 2b in which hydraulic jumps are possible: it follows that a steady downstream flow with Richardson number, $Ri_2 = 1/3$ is therefore stable both to KHI and to a possible hydraulic transition whatever the value, η_2 . To be consistent with the model’s assumption that $Ri_2 = 1/3$ a measured downstream Froude number should lie on (or at least be close to) the dotted line and be approximately equal to $6(1-\eta_2)$. Although, by comparing figures 2b and 2c, it is evident that KHI is possible where jumps may occur in all of region B and most of C, there is a small region marked E in figure 2c, part of C, where jumps are possible but KHI is not. (The flow with small values of η_1 is stabilized by the presence of the rigid boundary at $z = 0$, reducing the critical Richardson number to values below $1/4$.) The possibility of KHI where jumps occur in regions B and C implies that (unless the flow is in the region E) it might be difficult, if not impossible, when comparing model predictions to observations to distinguish between hydraulic transitions and those caused by KHI; the occurrence of turbulence and an associated change in flow profiles may be a consequence of a hydraulic transition or of KHI, and in this sense the two are synonymous. (It will however be shown in § 3 that in at least two cases the nature of the hydraulic transition is quite distinct from KHI.) In regions A and D of figure 2b, the upstream flow is liable to KHI but not to a hydraulic jump, in D because upstream waves are possible (figure 2a) and in A because no hydraulic jump solutions can be found; for flows in region A small amplitude KHI disturbances may grow, but no finite amplitude hydraulic transition is possible.

There is one factor that may distinguish hydraulic jumps from KHI. Where they occur the turbulent hydraulic jumps are stationary, their position fixed where the flow becomes supercritical, e.g., downstream of sills or constrictions in the width of channels. The conditions favouring the onset of KHI may similarly be determined by the topography, e.g., by its enhancement of shear. It is however a property of KHI that the disturbances following instability and developing into billows and subsequently turbulence, propagate downstream at a speed within the range of the flow speeds, i.e., so that a critical level exists. The billows propagate at a speed between that of the upper layer (zero in the model) and that of the lower layer, U_l , possibly causing the

critical position from which they develop, i.e., where the flow becomes subject to KHI (and possibly supercritical), to pulsate slightly in its downstream location.

As explained further in § 3 (and shown later in figure 6), the TL model provides prediction of other quantities related to transitions. The theory does not establish, however, the physical processes leading to the onset of turbulence in the transition. These might include an overturning billow-like structure or rotor (Ogden & Helfrich, 2016; e.g., their figure 4d of an internal bore) or KHI. Nor does the theoretical model describe the nature of the flow within the turbulent transition (although it has been supposed to have a character sufficiently far downstream where turbulence has collapsed similar to that following KHI, with $Ri_2 = 1/3$). Much about its structure is however revealed by observations described in § 3. The model does not predict the values of η or Fr within the turbulent transition region itself but these are determined from the observations. Some information is however available from the model about the mean rate of dissipation of turbulent kinetic energy as explained later, and estimates may be made of the vertical fluxes within the transition; Thorpe (2010).

Observations are used in §§ 3-5 to examine the predictions (and test the validity) of the theoretical model. Assumptions and approximations made in applying the theoretical model to observations are reviewed in appendix B. One of these is that rather than the uniform density of the η profiles, the observed density profiles may have a nearly constant gradient above the flowing layer near the seabed (e.g., as seen later in profiles in figure 4a). It is shown in appendix C that this appears unlikely to allow upward radiation of internal waves with energy and momentum loss from a transition region.

3. The Samoan Passage

3.1 *The observations*

Alford et al. (2013) examined the dense deep northerly flow through the Samoan Passage. They made detailed ‘tow-yo’ measurements with a CTD (measuring conductivity, temperature and depth) and a LADCP (a lowered acoustic Doppler current profiler) to obtain profiles of potential density, σ_{θ} , referenced to 4000 m, and velocity in a region of mean depth about 5100 m. The ‘tow-yo’ cycled between 40 m off the bottom and 4200 m depth making profiles with a derived 1 m vertical resolution about 250 m apart, and thus inclined at a mean angle to the horizontal of about 74 deg. Potential temperature and dissipation data over a major sill near 8° S are displayed in figure 3c in Alford et al.’s paper and are reproduced here in figure 3. Being at low latitude, the effects of the Earth’s rotation are likely to be relatively small. This section shows locations designated by their position, x (in kilometers), from 0 to 31.5. It passes in a northerly direction from just upstream (south) of the sill. Adjacent to the seabed an approximately 250 m thick layer of relatively dense water flows northwards about 0.4 m s^{-1} . It is capped by an interfacial layer in which the velocity and potential density decrease upwards. Above this the flow is relatively small. The analysis made here is of two subsections of the data where hydraulic transitions appear likely. § 3.2 describes $x = 20$ to 25, presented first because – as it appears from figure 3 – it is found to contain a single ‘cleanly defined’ hydraulic jump and consequently sets a standard for later analysis. § 3.3 is from $x = 3$ to 12 where a jump may also occur.

Additional measurements in the Samoan Passage are described by Voet et al. (2015, 2016).

3.2 The tow-yo section from 19 km to 25 km

Profiles of potential density and northwards velocity at 1 km spacing in the section of increasing depths from $x = 19$ to $x = 25$ are shown in figures 4a and 4b, respectively. Table 1 shows the results of fitting the η profiles to these data as described in appendix A. Here η (with no subscript) is derived from the best fit of an η profile to the observations at a position, x . The mean thickness, ηh , of the lower layer is 256 m and its mean northward speed is 0.43 m s^{-1} . The mean thickness of the interfacial layer is 274 m. With the estimated values of Fr and η , figure 2 (with $\eta_l = \eta$) is used to determine whether or not the flow at various positions, x , can support a hydraulic jump. Points in the (Fr, η) plane denoted by their position, x , are shown in figure 5a which is divided as in figure 2. At $x = 19$, the Froude number, $Fr = 2.1$ and $\eta = 0.64$, and (from figure 2b) the flow is subcritical (i.e., no hydraulic jump is possible). At $x = 20$, $Fr = 4.7$ and $\eta = 0.64$ and, as shown by the location of the point in figure 5a, according to the model the flow is supercritical with (figure 2b) a single solution for the downstream flow. The density profile contains few regions of static instability and there is a relatively low dissipation rate (figure 3).

Figure 6 (reproduced from TL's figure 5) shows contours of various downstream quantities derived from the model corresponding to upstream values, η_l and Fr . The predicted downstream values (at a location where $Ri \sim 1/3$) that correspond to upstream values η_l and Fr at $x = 20$ are $\eta_2 = 0.47$ (figure 6a) and $q = h_2/h_1 = 1.29$ (figure 6b). The latter has $q > 1$ and implies that the thickness of the overall flowing layer at the downstream location should exceed that upstream or, since at $x = 20$ the layer thickness is $h_1 = 426 \text{ m}$ (table 1), the predicted downstream value is $h_2 = 549 \text{ m}$. Moreover the predicted downstream thickness of the lower layer, $\eta_2 h_2$, is 258 m, i.e., the thickness of the uniform layer below the interfacial layer, should be less than that upstream, $\eta_l h_l = 271 \text{ m}$. Since the upper edge of the interfacial layer is predicted to increase in height above the bottom and the lower edge to decrease, a mode 2 transition from upstream to downstream of the transition is expected as noted in § 2. But, to comply with the model, does the flow attain an approximately steady subcritical state with $Ri_2 \approx 1/3$ at some $x > 20$?

Although there is a well-defined shear and density interface between 4670 m and 4790 m depth at $x = 21$, above it the density profile has a large region of static instability with variable shear at depths of 4530-4700 m, marked 'A' in figure 4a, and this x -location (the parameters of the interfacial region also implying in figure 5a that the flow is supercritical) is presumably within a hydraulic jump downstream of $x = 20$ following its supercritical state. At $x = 22$ there is a near uniform layer from 4520 m to 4750 m, marked 'B' in figure 4a, containing a 60 m high region of static instability. At $x = 23$, there is what appears to be an 80 m deep layer of residual overturn, 'C', near 4650 m. Evidence of this layer persists at $x = 24$, 'D'. The presence of the inversions (statically unstable regions) is reflected by the large uncertainty in Fr shown in table 1 and figure 5a at $x = 22$ and 23, and consequently the sub- or supercritical state of the flow is not definitely known at $x = 22$, although the latter is favored. However at $x = 24$ the flow becomes subcritical (although the interface in both density and velocity is somewhat irregular, possibly layered) with $Ri = 0.33$ ($\approx 1/3$) and a Froude number that approaches the dot-dash line in figure 2c, reproduced in figure 5a, as required in the model flow downstream of KHI.

The features of the jump described in the last paragraph are illustrated in more detail in the potential density contours of figure 7. The mixing region is outlined by an oval shaped curve to indicate its location and approximate dimensions. It is characterized by relatively uniform density but with frequent inversions. It begins near $x = 20$, the

position where the flow is first predicted to be supercritical. The mixing region appears initially near 4600 m depth, about 410 m off the bottom, splitting into two the upstream stratified interfacial layer between 4530 m and 4650 m. The potential density of the fluid where the mixed layer first appears is slightly less than the mean potential density in this interfacial layer. At $x = 22$ the layer develops into a vertically near-uniform region containing frequent density inversions extending from 4480 m to 4770 m depth. At $x = 23$, the centre of the mixing region is at 4650 m, about 485 m off the bottom. The density of the oval shaped mixing region increases with x as more dense water is entrained from the bottom layer. Overall the layer of mixing resembles a mid-water (i.e., separated by about 200 m from the bottom) 3.7 km long rotor-like structure following the gradual bottom slope, although no significant sustained flow in the upstream direction was recorded that might confirm the circulatory flow of a rotor. At its maximum the mixing layer is about 390 m in height, and its aspect ratio - height divided by length - is approximately 0.08. The velocity field is more uncertain and less firmly structured than the density, but the oval layer appears to have a generally weak flow above its stratified base below which the near-bed northerly flow continues at about 0.4 ms^{-1} . The mixing layer forming the hydraulic jump has a form reminiscent of a steady spilling surface-wave breaker (e.g., Rapp & Melville, 1990), like that downstream of a weir led by a ‘toe’ near $x = 20, z = 4600\text{m}$. There is no evidence that it is initiated by an overturn caused by convective instability (as in a plunging surface-wave breaker) or by KH billows, characterized e.g., by ‘braids’, high gradient regions between periodic billows, although the uniformity of the layer is sustained by static instability and convection. Its form is similar to that produced by breaking forced internal waves in the atmosphere above mountain ridges, modeled by Afanasyev & Peltier (1998; see especially their figure 12d) and by Yakovenko, Thomas & Castro (2011).

The values of η and h at $x = 24$ are 0.33 and 561 m, respectively, compared to the model’s predicted values of 0.47 and 549 m, respectively, for a jump produced by the flow at $x = 20$. The lower layer thickness at $x = 24$ is 186 m, less than the predicted 258 m, but at least showing that the transition is of mode 2, as predicted. In view of the assumptions made in the theoretical model, of the uncertainty in fitting the η profiles to data (reflected in the error bars of figure 5a), of whether the profiles at $x = 20$ represent the flow conditions immediately before the transition, and of the unaccounted-for variations in bottom topography shown in figure 3 over the horizontal extent of the transition layer shown in figure 7, it is not surprising that the predicted values differ somewhat from the observed. The density within the interfacial layer is irregular and ‘step-like’ at $x = 25$ (figure 4a). At this location, however, the northward velocity of the flow above the interfacial layer is about 0.1 m s^{-1} , violating the model’s assumption of zero flow.

Contours of a non-dimensional energy loss in the jump, E_n , in (Fr, η_1) space, estimated by TL (their equation 4.3), are given by figure 6c. E_n is related to the mean rate of dissipation of turbulent kinetic energy per unit mass in the hydraulic jump, ε , by

$$\varepsilon = E_n U_l^3 (1 + 3\eta_1) / \{4L_j[(1 - \eta_1) + q(1 - \eta_2)]\}, \quad (6)$$

where L_j is the horizontal extent of the transition region associated with the hydraulic jump, $q = h_2/h_1$, and U_l ($\approx 0.43 \text{ m s}^{-1}$) is the speed of the lower layer upstream of the jump. Using the upstream values of η_1 and Fr at $x = 20$, figure 6c gives $E_n \approx 0.035$. Selecting the downstream value of η_2 as that at $x = 24$, and choosing $L_j = 4 \text{ km}$ (the

separation distance between the upstream and downstream locations) gives a mean value, $\varepsilon = 4.1 \times 10^{-7} \text{ W kg}^{-1}$. This is comparable to the values observed and given in Alford et al.'s figures 2 and 3c, the latter reproduced here in figure 3. A further comparison of theory and data is made in appendix D: the approximate time required for turbulence to collapse is consistent with the observations of the length of the active mixing region estimated to be approximately $6U_I N^{-1}$, where N is the mean buoyancy frequency of the stratified region surrounding the upstream interfacial layer.

In summary: a transition begins at $x = 20$, the location where, according to the model, the flow becomes supercritical, and it takes the form of an elongated mixing layer. If this is a rotor it is similar to those found in numerical studies of moving bores by Ogden & Helfrich (2016). It is separated from the seabed by a relatively strong down-slope bottom flow, and thus differs from the near-boundary rotors found in large internal waves in the lee of mountains described by Scorer (1972; e.g., his figure 5.7.i) and Doyle & Durran (2007). No KH billows or braids are apparent in the tow-yo profiles immediately downstream of $x = 20$.

3.3 The tow-yo section from 3km to 12 km

Table 2 and figure 5b show the results of fitting the η profiles to data in $3 \leq x \leq 12$. The mean thicknesses, the averages of ηh and h of the other flowing layers between $x = 3$ and $x = 12$ are 283 m and 484 m, respectively, and the mean northward speed of the dense lower layer is 0.30 ms^{-1} . However at $x = 7$, the flow is unusually small, less than 0.05 ms^{-1} , throughout the depth range sampled by the tow-yo. Although the density profile was 'normal', with a well-defined interfacial layer between depths of about 4300 m and 4700 m, no northward-going lower layer appears in the velocity profile. We have no simple explanation for this and it was not possible to fit consistent η profiles to both velocity and density.

According to the model the flow becomes supercritical at $x = 4.8$, returning to subcritical at $x = 5.8$. As shown in the contours of potential density in figure 8 a 100 m high structure with numerous density inversions outlined by the oval shaped curve appears in the flow at $x = 4.8$. Its density is approximately equal to the mean of that in the upstream interfacial layer and it divides this layer into two. This mixing region extends approximately 1 km downstream, ending at $x \approx 5.8$, the location at which the flow returns to a subcritical state. The aspect ratio of the mixing region is about 0.1 compared with 0.08 for the transition at $x = 20$ shown in figure 7. Its length as predicted in appendix D is $6U_I N^{-1} \approx 1.5 \text{ km}$ rather than the 1 km observed. Other mixing layers appear beyond $x = 5.8$, e.g. near $x = 6.1$, $z = 4680 \text{ m}$, where, according to the model, the flow is subcritical but downstream of substantial increases in water depth.

Using the values of η and Fr at $x = 4.8$ as those upstream of a transition, figure 6a predicts $\eta_2 \approx 0.57$ downstream. This compares fairly well with the observed value, 0.53, at the subcritical downstream end of the mixed structure at $x = 5.8$. The Richardson number at $x = 5.8$ is however 0.48, indicating a stable flow, but greater than the value, $Ri_2 = 0.33$, adopted in the model. The value of E_n determined from figure 6c at $x = 4.8$ is approximately 0.018. The mean value of ε in the 1 km between $x = 4.8$ and 5.8 derived using (6) is approximately $1.0 \times 10^{-6} \text{ W kg}^{-1}$, in order of magnitude accord with the values shown in figure 3. Although smaller than the feature associated with the hydraulic jump at $x = 20$ the mixed structure shares many of its general characteristics, including its being separated from the seabed by the near bottom northerly flow of dense water and by an absence of any clear evidence of KH billows or braids.

4. The Red Sea outflow

A different Froude number, described as a ‘bulk Froude number’ and denoted here by Fr_P , is used by Peters et al. (2005) in the analysis of data from the Red Sea Outflow in the Gulf of Aden, a near bottom flow with velocity and density structure similar to the profiles considered in the Samoan Passage. In terms of the notation of § 2, Peters et al. define Fr_P “following discussion with J. Price 2003 (personal communication)” by

$$\begin{aligned} Fr_P^2 &= (U_I/2)^2 / \{g\Delta[\eta_I h_I + h_I(1-\eta_I)/2]\}, \\ &= U_I^2 / [2g\Delta h_I(1+\eta_I)], \end{aligned} \quad (7)$$

or, in terms of Fr given by (5) and the local value, η_I ,

$$Fr_P^2 = Fr/[2(1+\eta_I)]. \quad (8)$$

The critical curves in the (η_I, Fr) plane shown in figure 2 are translated to the (η_I, Fr_P) plane in figure 9. The thick line represents the lowest values of Fr_P at which, according to the model described in § 2, a hydraulic transition can occur for given η_I ; values of the minimum Fr_P vary with η_I . The smallest Fr_P at which transition can occur is 0.80 at $\eta_I = 0.74$. The minimum (or critical) Fr_P is equal to unity only when $\eta_I = 0.6$.

The Red Sea Outflow exits the Red Sea through the Strait of Bab el Mandeb and passes down two channels in the Gulf of Aden between 12° N and 12°30' N, the northern and southern channels denoted by Peters et al. (2005) as NC and SC, respectively. The outflow, confined to the channels, is conceived by Peters et al. (2005) and Peters & Johns (2005) in terms of gradually entraining plumes of dense water rather than gravity currents and in which the spread is dominated by localized hydraulic jumps. Measurements are made using a package combining an LADCP and CTD. During the period of stronger flow in observations made in winter, values of Fr_P estimated by Peters & Johns (2005) have locally maximum values of about 0.93 and 0.97 at down-channel distances in the NC of about 70 and 120 km, respectively, from the Strait of Bab al Mandeb, and 0.88 at about 60 km in the SC. At all three locations the rate of dissipation of turbulent kinetic energy, estimated using an assumed proportionality between the Ozmidov and Thorpe length scales, is also maximal, suggesting the possible presence of hydraulic jumps. At these locations the value η_I , taken here as the ratio of the bottom layer to the total thickness of the flowing layer (H_b/H_p in the notation of Peters & Johns, 2005) is approximately 0.30 and 0.27 in the NC, and 0.42 in the SC, respectively. The corresponding points in the (Fr_P, η_I) plane are shown in figure 9a and indicate that, although the values of Fr_P exceed the minimum for hydraulic jumps to occur, the flows should be sub-critical, stable to hydraulic jumps at the estimated η_I . Values are however uncertain. Peters et al. and Peters & Johns take the depth of the lower layer (ηh , or H_b in their notation) as the height above the seabed at which the downstream velocity is a maximum, less than the estimate of $\eta_I h$ determined as in appendix A. The total thickness of the flowing layer (H_p in their notation), is taken in a less precise way, depending on the speed or direction of the velocity, or on the salinity. The value $\eta_I = H_b/H_p$, is likely to be less than that found as in appendix A, and Fr_P may consequently be overestimated. There is no clear evidence from observations or theory of the presence of hydraulic jumps in the Red Sea outflow. Rather, the spreading of the outflow down the channels

in the Gulf of Aden appears to be dominated by a more gradual process of turbulent entrainment as concluded by the two sets of authors.

5. The Mediterranean outflow

Gasser et al. (2011) and Nash et al. (2012) report observations using moorings and tow-yos in the Mediterranean outflow in the Gulf of Cadiz 70 km west of the Strait of Gibraltar and to the west of the Espartel Sill, the most western sill of the Strait. At this location the dense outflow is confined to a westward flowing layer of water, some 150 m thick and of relatively high salinity, moving westward over the seabed at approximately 1.2 m s^{-1} . Profiles of density and velocity are derived from surface to the bottom with 1 km horizontal resolution. Flow in the layer overlying the outflow is of order 0.2 m s^{-1} to the east. Gasser et al. (2011) show roughly 10 km long downstream tow-yo sections of salinity, downstream velocity and gradient Richardson number at four stages of the M_2 tidal cycle. Nash et al. (2012) present a tow-yo section of downstream velocity and $\log \varepsilon$ at the same time as that of the low tidal flow section presented by Gasser et al., and focus attention on two stations in the section, separated by about 3.5 km, UTS (upstream at $6^\circ 19.23'W$, $35^\circ 47.04'N$, where the water depth is approximately 417 m) and DTS (downstream at $6^\circ 21.00'W$, $35^\circ 46.51'N$, in 454 m).

Following Peters et al. (2011), Nash et al. use the bulk Froude number, Fr_p , in their analysis, but assume, without formal justification, that transition occurs at $Fr_p = 1$. At UTS, 90% of the estimates of Fr_p lie between 0.70 and 0.92 (with a mean of 0.81). The mean dissipation, ε , in the outflowing layer is about $1 \times 10^{-6} \text{ W kg}^{-1}$. The value of η estimated from the profiles given by Gasser et al. and Nash et al. is 0.45 ± 0.03 . Respective points are shown in figure 9b. They indicate that, according to the model, the flow is sub-critical and stable to a hydraulic transition at UTS.

About 1-2 km west of UTS Nash et al. (2012; their figure 3, b&c) find a notable increase in the high frequency displacement of isopycnals, an increase in interface thickness, and a rise in ε to a mean value of about $1 \times 10^{-5} \text{ W kg}^{-1}$ in the outflow, suggesting that a mode 2 transition has occurred. Further downstream at DTS the mean $Fr_p = 0.99$ and 90% of the estimates of Fr_p lie between 0.63 and 1.45, 45% having $Fr_p > 1$, and η is equal to 0.39 ± 0.03 . As shown in figure 9b, the upper values of these estimates of Fr_p and η imply that a hydraulic jump is possible. It is likely, however, that conditions for a jump have been reached upstream of DTS and that DTS lies within the transitional region, this accounting for the relatively large variations in isopycnal depths and in Fr_p or Fr . Similarly large variations in Fr are observed downstream of the hydraulic jump at $x = 20 - 21$ in the Samoan Passage, figure 5a. (Taking the upper values at DTS, $Fr_p \approx 1.45$ and $\eta \approx 0.4$, we find $Fr = 5.85$ from (8) while figure 6 gives $\eta_2 \approx 0.3$, $q \approx 0.8$ and $E_n \approx 0.05$. Taking L_j equal to the distance between the two stations, i.e., 3.5 km, and using (6), gives $\varepsilon \approx 1.2 \times 10^{-5} \text{ W kg}^{-1}$, consistent with the observed dissipation rate at DTS.) Nash et al. use the Taylor-Goldstein equation to examine the stability of the flow at DTS to KHI. The gradient Richardson number of the flow near the centre of the interface above the flowing layer is less than $1/4$, and the flow is found to be unstable to KHI, consistent with the larger values of Fr_p being in region C of figure 9b. Downstream (to the west) of DTS the depth of the seabed increases sharply to about 500 m, resulting in an increase of η to about 0.5, a flow that exhibits 30-50 m overturns and ε exceeding $10^{-5} \text{ W kg}^{-1}$, again suggestive of a hydraulic jump.

6. Discussion

The η profiles defined by (2) provide an approximate, if imperfect, description of the continuous profiles of density and velocity found in near-bottom flows through the channels of the Samoan Passage and the outflows from the Red Sea and the Mediterranean. The predictions of the model described in § 2 are used to determine whether flows observed in these three regions are sub- or supercritical to stationary hydraulic transitions.

The majority of selected examples, including those in which hydraulic transitions are suspected in the Red Sea Outflow because of high values of turbulent dissipation (§ 4), appear to be subcritical within the uncertainty of the estimated η and Fr or Fr_P . (High turbulent dissipation may be caused by the stress generated by the rapid flow over a possibly rough seabed, a factor not accounted for in the model.) Downstream of two locations in the Samoan Passage ($x = 20$ and 4.8 ; figures 5a and 5b, respectively), the flow appears to have undergone a transition, and the consequent changes appear to be reasonably in accord with the model's predictions, including that of the dissipation of turbulent kinetic energy. The transition is manifest as a downstream-elongated mid-water actively mixing region. Its form downstream of the position at which flow becomes supercritical is most clearly seen in the potential density field of figure 7. A likely hydraulic jump is identified in the Mediterranean Outflow between Nash et al.'s stations UTS and DTS (§ 5) but none in the outflow from the Red Sea in the Gulf of Aden, in accord with analysis by Peters et al. (2005) and Peters & Johns (2005) (§ 4).

Further to the discussion in § 2, it is of note that only in the possibly rare cases where η is small and Fr large (region E in figure 2c) does the model predict that internal hydraulic jumps occur but not KHI. One case (at $x = 9$ in the Samoan Passage, figure 5b and table 2) is found, however, in which the flow is unstable to KHI but apparently not liable to a hydraulic transition (i.e., regions A or D in figure 2b).

There is a further possibility not accounted for in the model: that the features identified from the tow-yo data as hydraulic jumps or KHI are not stationary, but are propagating down-slope as internal roll waves similar to those reported by Fer, Lemmin & Thorpe (2002). This is however unlikely as later observations in the Samoan Passage analysed by G.Voet have found very similar jump structures in the same locations. For example, figure 10 shows the hydraulic jump near $x = 20$ surveyed about 2 years after that shown in figure 7. The overall structure outlined by the oval curve remains generally the same, with comparable height and length but with an aspect ratio of about 0.06. The mixing layer splits the upstream interfacial layer into two, and the mean density in the layer increases with x , although less rapidly in figure 10 than in figure 7. The depth of the toe in figure 10 is about 100 m deeper than in figure 7 and it is about 500 m further downstream. Although Yakovenko, Thomas & Castro (2011) draw attention to the long period vacillation of lee wave systems and mixing near a topographic feature, there is no evidence here of such variability, only that the feature persists. The theory of Rottman, Broutman & Grimshaw (1996) supporting variability finds that it is mainly due to internal waves that persist near the topography, but occasionally propagate upstream, a feature excluded in the present hydraulic jump model.

The Earth's rotation is disregarded in the model. Its effect on the hydraulic jumps illustrated in figures 7 and 8 may be assessed by the magnitude of a Burger number, Bu . This is equal to the ratio of the internal Rossby radius of deformation, NH/f ,

divided by the extent of the mixing region, L_j , where N is the mean buoyancy frequency of the fluid in which the jump occurs, H is the thickness of the mixing layer produced by the jump, and f is the Coriolis frequency, $2.03 \times 10^{-5} \text{ s}^{-1}$, at the latitude of the Samoan Passage. Estimated values of Bu are 3.1 ± 1.4 and 4.2 ± 0.3 for the jumps at $x = 20$ and 4.8 , respectively. These values exceed unity and indicate that here in the Samoan Passage, although not necessarily in the Red Sea or Mediterranean outflows, rotation has a relatively unimportant effect in the region downstream of a transition.

7. Conclusions

Available observations are largely consistent with the predictions of the model sketched in figure 1 and summarized in figure 2. The prediction of hydraulic transitions might, however, be refined and more closely tested by selecting a model with, instead of η profiles, velocity and density profiles that better match those observed, as in Thorpe (2010). The transition downstream of $x = 20$ in the Samoan Passage provides a well-defined example of a hydraulic jump in the deep ocean and of the consequent changes in density (figure 4). The jump appears to be persistent and possibly quasi-steady, being found in observations made two years apart (figures 7 & 10). It takes the form of a large, near-uniform, mixing layer that splits the upstream interfacial layer overlying the deep dense layer of flowing water. This mixing region commences at a ‘toe’ (like that of a spilling surface-wave breaker) at which neither KHI nor convective instability is evident although static and convective instability are present within the mixed layer itself. The mixed layer produced by the transition is similar in form to those ascribed to the breaking of internal waves in the lee of mountain ridges in the atmosphere.

It is likely that a variety of types of hydraulic transitions are possible in stratified shear flows. A similar ‘nearly stagnant isolating layer’, some 50 m thick and preceded by flow bifurcation, is observed in the relatively shallow water flow over the sill in the Knight Inlet, British Columbia (Farmer & Armi, 1999; Winters & Armi, 2014; Jagannathan, Winters & Armi, 2017). The formation of a near-uniform layer therefore appears to be a characteristic of at least some internal hydraulic jumps. Gasser et al. (2011) provide one example of changes in the Mediterranean Outflow downstream of their station UTS occasioned at one phase of the tidal cycle by the presence of 50 m high and 1 km long KH billows. Billows have an important role in the atmospheric jump in the lee of the US Sierra Nevada mountain range (Armi & Mayr, 2011). More detailed observations are desirable to provide further examples of hydraulic jumps that might allow their classification particularly where, according to the model, both KHI and hydraulic jumps are possible as described in § 2.

Acknowledgements

We acknowledge and salute the effort required to collect and analyse the data referred to in this study, particularly by those whose contribution is recognized by Alford et al. (2013). Data from the Samoan Passage were collected under National Science Foundation Grants OCE-1029268 and OCE-1029483. The help of Mrs Kate Davis in the preparation of figures is gratefully acknowledged.

Appendix A. Fitting model to data

Data from the Samoan Passage used for analysis are listed profiles of the northward component of velocity and the potential density referenced to 4000 m at 1 m vertical

intervals obtained by tow-yos. Examples at approximately 1 km horizontal separations are shown in figure 4. The interfacial layer in the velocity profiles is generally more clearly defined than that of the density. (The suffixes, i , in η_i etc. are presently dropped, making no assumptions about whether locations are upstream or downstream of a jump.) At a chosen location (in km) a line is fitted to the velocity profile to represent the velocity interface. This intersects zero velocity at a determined height $z = h$ above the seabed. The mean velocity, U , below the interface generally shows evidence of a frictional bottom boundary layer but is simply fitted by a line, $U = \text{constant}$, meeting the constant gradient line at $z = \eta h$, so defining a value of η and the velocity η profile. The velocity gradient is $U/[h(1 - \eta)]$. The difference in densities, $2\Delta\rho_0$, at level ηh and at level h are used to find the density gradient $2\Delta\rho_0/[h(1 - \eta)]$. The gradient Richardson number in the interfacial layer ($\eta h < z < h$) is $Ri = 2g\Delta h(1 - \eta)/U^2$, and represents and approximately preserves the minimum Richardson number of the observed flow. The Froude number of the upstream flow is $Fr = U^2/(g\Delta h) = 2(1 - \eta)/Ri$.

The maximum potential density of the lower layer in this section from the Samoan Passage (at least at 40 m above the seabed, the lower limit of the tow-yo cycles) remains fairly constant, showing that the water at this level is not mixed with the overlying less dense water. (This implies that the parameter δ appearing in TL is unity.) The speed of the lower layer however changes as a consequence of its expansion or contraction as it passes downstream.

Values of η and Fr at numbered x locations in Alford et al.'s (2013) data are shown in tables 1 & 2 and figures 5 & 6.

622

623 **Appendix B. Assumptions of the theory**

624

The hydraulic jump theory (§ 2 and TL) makes a number of assumptions about the real flow that are only approximately satisfied. It is assumed in the model that the velocity upstream and downstream of the stationary hydraulic jump or transition is uniform in a horizontal direction and depends only on the vertical coordinate, z . In reality, the seabed generally slopes (in the Samoan Passage descending from a depth about 4706 m at $x = 4$ to 5128 m at $x = 25$, a mean gradient of 1.15° , but crossing notable sills at $x = 4$ and 19 and a trough at $x = 7$ in addition to smaller scale undulations; see figure 3). The real flow is consequently not steady, as assumed, but tends to accelerate down-slope, subject to the balance between the down-slope component of gravity and the bottom and interfacial drag. It will also respond to changes in channel width and to the tides (although in the Samoan Passage these are relatively weak, less than 0.05 ms^{-1}). Since at the latitude of the Passage, 8° S , the inertial period is about 86 hrs and the time required to complete the tow-yo section of figures 4 or 7 made at 0.25 ms^{-1} is less than 6 hrs, inertial oscillations (which have moderate amplitude, typically less than 0.15 ms^{-1}) will contribute little to the changes that are apparent in this section. The model's velocity and density profiles are supposed similar in shape, and the velocity is zero above the interfacial layer. In reality changes in the flow occur continually both inside and outside the transition region. The density and velocity profiles are similar in that they generally contain an interfacial region of high gradient at the same depths, but (i) the flow above the shear layer is not precisely zero, although generally relatively small (an exception being at $x = 25$ in the Samoan Passage), and (ii) the potential density in the region above the shear layer is not constant but generally has a negative (i.e., statically stable) gradient. This may be sufficiently small to prevent the upward radiation of internal waves (see

appendix C). The effects of stationary (possibly breaking; Yakovenko, Thomas & Castro, 2014) lee waves generated by the flow over the sill are not taken into account and the transition is not allowed to be undular in form. In the model it is assumed that turbulence in the hydraulic jump collapses to give a Richardson number of about 1/3 as observed in laboratory and numerical experiments of KHI. The transition occurs over a level horizontal seabed. In reality Richardson numbers of approximately 1/3 are found downstream of possible jumps, e.g., at $x = 24$ and at 5.8 and 11 in tables 1 & 2, respectively. Further study is required to extend the simple local model to a broader range of conditions.

Appendix C. Radiation of internal waves

Waves radiating upwards from a hydraulic jump transition region may be forced by KH billows (and other disturbances forced by turbulence) in the hydraulic transition region. The fastest growing KHI disturbances in an η profile move downstream at a speed of about $U/2$ and have a wavelength of about 7 times the interface thickness, $h(1-\eta)$ (Miles & Howard, 1963). Suppose, for generality, that the hydraulic jump contains perturbations of horizontal scale, λ , moving downstream at speed $c \sim U/2$, and that these generate internal waves in an overlying region of buoyancy frequency, N . If the frequency of the internal waves is σ and their horizontal and vertical wavenumbers are $k = 2\pi/\lambda$ and m , respectively, then $\sigma/k = c$ and

$$\sigma^2 = N^2 k^2 / (k^2 + m^2), \quad (\text{A1})$$

the dispersion relation, disregarding the effect of the Coriolis force. This gives $m = \pm k(N^2/\sigma^2 - 1)^{1/2}$, which is real if $N/\sigma = N/c k > 1$. Waves can radiate upwards from the turbulent transition region if m is real or are evanescent, decaying exponentially upwards, if m is imaginary.

With the observed values in the Samoan Passage at $x = 3 - 12$ (or 19 - 25) of $c = U/2 = 0.15$ (or 0.21) m s^{-1} , $N = 4.62 \times 10^{-4}$ (or 4.79×10^{-4}) s^{-1} (greatly exceeding the inertial frequency, about $2.03 \times 10^{-5} \text{ s}^{-1}$) and with $k = 2\pi/[7h_I(1-\eta_I)]$ corresponding to KH billows, we have $k = 4.47 \times 10^{-3}$ (or 3.28×10^{-3}) m^{-1} giving $N/c k = 0.69$ (0.70). These values are less than 1, so that the forced waves are evanescent, trapped near the top of the flowing layer. The billow wavelengths, $\lambda = 7h_I(1-\eta_I) \sim 1.41$ (1.92) km, are a substantial fraction of, or exceed, the approximate length of transitions, 1.0 km (3.9 km) estimated in § 3.3 (§ 3.2). Only waves with horizontal wavelengths $> 2\pi c/N \sim 2.0$ (or 2.8) km may radiate upwards from the turbulent hydraulic transition, leading to a loss in energy and momentum. (A study of internal waves in the Samoan Passage by G.Voet finds that waves appear to be trapped in the lower layer and do not radiate much energy beyond the interfacial layer.)

Appendix D. The collapse of turbulence in the hydraulic jump

According to laboratory experiments of Thorpe (1973), the time for turbulence to collapse following KHI and to reach a state in which $Ri \sim 0.33$ (after which there is little change in layer thickness) is approximately given by $\tau = 6U_I/g\Delta$. (The flow may still continue to contain ‘striations’, remnants of turbulent overturns, beyond a time, $\tau_I = 12U_I/g\Delta$. The time for the decay of available potential energy in the turbulence or of the evolution of the efficiency parameter, Γ , in numerical calculations of Smyth, Moum & Caldwell, 2001, are consistent with a time τ_I , rather than the smaller, τ .)

Supposing that turbulence is advected downstream at a mean speed $U_I/2$, the distance downstream from a jump or ‘KHI event’ to where the gradient Ri becomes equal to $1/3$ is approximately $\tau U_I/2 = 3.5h_I Fr$. Using values at $x = 20$, the distance downstream before the flow evolves to a mean Richardson number of about $1/3$ is therefore approximately 6 km, somewhat greater than the distance between the observations at $x = 20$ and 24 or over the horizontal extent of the transition event shown in figure 7. The larger time, τ_I , suggests that remnants of the turbulence from a transition near $x = 20$ may be carried to at least 12 km downstream, and the irregular structure remaining in the observed interface at $x = 25$ is evidence that this may be so.

An alternative, again approximate, derivation of a collapse time but better representing that from a statically unstable region, is found from the laboratory study by Lawrie & Danziel (2011) of the decay of turbulence when an initially statically unstable region spreads into stably stratified surroundings with uniform buoyancy frequency, N . Shear is however absent. The decay time is approximately $12N^{-1}$. Taking $N \approx 6.2 \times 10^{-4} \text{ s}^{-1}$ to represent the stratification in the water surrounding the mixing layer at A – D in figure 4a, gives a decay time of approximately $2 \times 10^4 \text{ s}$ or, if water is carried at mean speed $U_I/2 \approx 0.215 \text{ ms}^{-1}$, a decay distance $6U_I N^{-1}$, of 4.2 km which is more consistent with that observed.

References

- AFANASYEV, YA.D., & PELTIER, W.R. 1998 The three-dimensionalization of stratified flows over two-dimensional topography. *J. Atmos. Sci.* **55**, 19-39.
- ALFORD, M. H., GIRTON, J. B., VOET, G., CARTER, G. S., MICKETT, B. & KLYMAK, J. M. 2013 Turbulent mixing and hydraulic control of abyssal water in the Samoan Passage, *Geophys. Res. Letts.* **40**, 4668-4674, doi:10.1002/grl.50684,2013.
- ARMI, L. & MAYR, G.T. 2011 The descending stratified flow and hydraulic jump in the lee of the Sierras. *J. Appl. Meteor. Climatol.* **50**, 1995-2011.
- BAINES, P.G. 1995 *Topographic effects in stratified flows*. Cambridge University Press, Cambridge, 482 pp.
- BAINES, P.G. 2016 Internal hydraulic jumps in two-layer systems. *J. Fluid Mech.* **787**, 1-15.
- DOYLE, J.D. & DURRAN, D.R. 2007 Rotor and subrotor dynamics in the lee of three-dimensional terrain. *J. Atmos. Sci.* **64**, 4202-4221.
- FARMER, D.M. & ARMI, L. 1999 Stratified flow over topography: the role of small-scale entrainment and mixing in flow establishment. *Proc. R. Soc. Lond. A* **455**, 3221-3258.
- FER, I., LEMMIN, U. & THORPE, S.A. 2002 Winter cascading of cold water in Lake Geneva. *J. Geophys. Res.* **107**, C6, 10.1029/2001JC000828, 2002.
- GASSER, M., PELEGI, J. I., NASH, J. D., PETERS, H. & GARCIA-LAFUENTE, J. 2011 Topographic control on the nascent Mediterranean outflow. *Geo.-Mar. Lett.* **31**, 301-314.
- JAGANNATHAN, A., WINTERS, K.B. & ARMI, L. 2017 Stability of stratified downslope flows with an overlying stagnant isolating layer. *J. Fluid Mech.* **810**, 392-411.
- LAWRIE, A.G.W. & DALZIEL, S.B. 2011 Rayleigh-Taylor instability in an otherwise stable stratification. *J. Fluid Mech.* **688**, 507-527.
- MILES, J. N. & HOWARD, L. N. 1963 Note on a heterogeneous shear flow. *J. Fluid Mech.* **20**, 331-336.

- NASH, J. D., PETERS, H., KELLY, S. M., PELEGRI, J. L., EMELIANOV, M. & GASSER, M. 2012 Turbulence and high-frequency variability in a deep gravity current outflow. *Geophys. Res. Letts.* **39**, L18611, doi:10.1029/2012GL052899, 2012.
- OGDEN, K. A. & HELFICH, K. R. 2016 Internal hydraulic jumps in two-layer flows with upstream shear. *J. Fluid Mech.* **789**, 64-92.
- PETERS, H. & JOHNS, W. E. 2005 Mixing and entrainment in the Red Sea outflow plume. Part II: turbulence characteristics. *J. Phys. Oceanogr.* **35**, 584-600.
- PETERS, H., JOHNS, W. E., BOWER, A. S. & FRATANTONI, D. M. 2005 Mixing and entrainment in the Red Sea outflow plume. Part I: plume structure. *J. Phys. Oceanogr.* **35**, 569-583.
- PETTRÉ, P. & ANDRÉ, J.-C. 1991 Surface pressure change through Loewe's phenomena and kitabatic flow jumps: study of two cases in Adélie Land, Antarctica. *J. Atmos. Sci.* **48**, 557-571.
- POLZIN, K., SPEER, K. G., TOOLE, J. M., & SCHMITT, R. W. 1996 Intense Mixing of Antarctic Bottom water in the Equatorial Atlantic Ocean. *Nature* **380**, 54-56.
- RAPP, R.J. & MELVILLE, W.K. 1990 Laboratory measurements of deep water breaking waves. *Phil. Trans. R. Soc. Lond. A* **331**, 735-800.
- ROTTMAN, J.W., BROUTMAN, D. & GRIMSHAW, R. 1996 Numerical simulations of uniformly stratified fluid flow over topography. *J. Fluid Mech.* **306**, 1-30.
- SCORER, R. 1972 *Clouds of the World*. David & Charles (Publishers) Ltd., Newton Abbot, Devon, UK. 176 pp.
- SMYTH, W. D., MOUM, J. N. & CALDWELL, D. R. 2001 The efficiency of mixing in turbulent patches: inferences from direct simulations and microstructure observations. *J. Phys. Oceanogr.* **31**, 1969-1992.
- THORPE, S. A. 1973 Experiments on instability and turbulence in a stratified shear flow. *J. Fluid Mech.* **61**, 731-751.
- THORPE, S. A. 2010 Turbulent hydraulic jumps in a stratified shear flow. *J. Fluid Mech.* **654**, 305-350.
- THORPE, S. A. & LI, L. 2014 Turbulent hydraulic jumps in a stratified shear flow; part II. *J. Fluid Mech.* **758**, 94-120 (referred to as 'TL').
- VOET, G., GIRTON, J. B., ALFORD, M. H., CARTER, G. S., KLYMAK, J. M. & MICKETT, J. B. 2015 Pathways, volume transport, and mixing of abyssal water in the Samoan Passage. *J. Phys. Oceanogr.* **45**, 562-588.
- VOET, G., ALFORD, M. H., GIRTON, J. B., CARTER, G. S., MICKETT, J. B. & KLYMAK, J. M. 2016 Warming and weakening of the abyssal flow through the Samoan Passage. *J. Phys. Oceanogr.* **46**, 2389-2401.
- WINTERS, K.B. & ARMI, L. 2014 Topographic control and stratified flows: upstream jets, blocking and isolating layers. *J. Fluid Mech.* **753**, 80-103.
- YAKOVENKO, S. N., THOMAS, T. G. & CASTRO, I. P. 2011 A turbulent patch arising from a breaking internal wave. *J. Fluid Mech.* **677**, 103-133.
- YAKOVENKO, S. N., THOMAS, T. G. & CASTRO, I. P. 2014 Transition through Rayleigh-Taylor instabilities in a breaking internal lee wave. *J. Fluid Mech.* **760**, 466-493.

Tables

799
800
801
802
803
804
805
806
807
808
809

TABLE 1

Location	Depth	h	η	Ri	Fr	Super/sub critical
x (km)	(m)	(m)				
19	5022	537	0.64 ± 0.04	0.35	2.1 ± 0.2	sub
20	5006	426	0.64 ± 0.03	0.15	4.7 ± 0.5	super
21	5038	383	0.57 ± 0.03	0.11	8.0 ± 0.8	super
22	5092	432 - 617	0.44 ± 0.04	0.17 ± 0.13	6.7 ± 2.5	uncertain
23	5140	520 ± 45	0.54 ± 0.03	0.11 ± 0.10	8.7 ± 2.4	super
24	5076	561	0.33 ± 0.02	0.33	4.1 ± 0.4	sub
25	5111	521	0.31 ± 0.02	0.24	5.7 ± 0.60	uncertain

810 Table 1. Values derived from fitting η profiles to data at locations of $x = 19$ to 25 in
811 the Samoan Passage. The possible errors in the estimates of η and Fr (and of h and Ri
812 at $x = 22$ and 23) are indicated by ‘ \pm ’ or a range of values. Locations where the range
813 of possible values crosses the subcritical – supercritical boundary are labeled
814 ‘uncertain’.

815

816

TABLE 2

Location	Depth	h	η	Ri	Fr	Super/sub critical
(km)	(m)	(m)				
3	4776	458	0.85 ± 0.04	0.30	0.98 ± 0.1	sub
4	4706	344	0.75 ± 0.04	0.31	1.6 ± 0.2	sub
4.2	4706	291	0.74 ± 0.04	0.31	1.7 ± 0.2	sub
4.5	4753	338	0.72 ± 0.04	0.32	1.8 ± 0.2	sub
4.8	4756	356	0.65 ± 0.04	0.22	3.3 ± 0.2	super
5.1	4803	378	0.60 ± 0.05	0.24	3.3 ± 0.5	uncertain
5.4	4805	355	0.58 ± 0.04	0.18	4.6 ± 0.2	super
5.8	4889	409	0.53 ± 0.05	0.48	1.9 ± 0.2	sub
6.1	4888	538	0.35 ± 0.1	1.0	1.3 ± 0.07	sub
7	4952	***				
8	4936	596	0.43 ± 0.09	1.5	0.78 ± 0.33	sub
9	4856	431	0.75 ± 0.03	0.20	2.2 ± 0.05	uncertain
10	4904	454	0.59 ± 0.03	0.39	2.1 ± 0.2	sub
11	4920	470	0.57 ± 0.03	0.33	2.5 ± 0.04	sub
12	4952	562	0.57 ± 0.04	0.45	1.9 ± 0.2	sub

834

835 Table 2. Values derived from fitting η profiles to data at locations of $x = 3$ to 12 in the
836 Samoan Passage. The uncertainty in the estimates of η and Fr are indicated by ‘ \pm ’. At
837 $x = 7$ (marked ***), the flow is small, less than 0.1 ms^{-1} , perhaps being blocked, and it
838 was not possible to fit consistent η profiles to both velocity and density. At $x = 9$ the
839 flow is marginal (i.e., on or very close to the supercritical-subcritical boundary in
840 figure 4b) although unstable to KHI.

841

842

843

Figure captions

844

845 1. A sketch showing the model representation of a turbulent hydraulic jump or
846 transition in a stratified shear flow over a plane boundary at $z = 0$. (a) represents a
847 mode 1 transition and (b) a transition of mode 2. Q and Q_i represent the fluxes of
848 volume of density $\rho_0(1 - \Delta)$ from above and of density $\rho_0(1 + \Delta)$ from below into the

849 transition zone. (From Thorpe & Li, 2014; their figure 1.)

850

851 2. A summary of the stability of a flow and hydraulic jumps in the (η_1, Fr) plane. (a):

852 Internal waves can propagate upstream in the hatched region, and consequently no

853 stationary hydraulic jumps are formed here. $Ri = 1/4$ on the line joining $(\eta_1 = 0, Fr = 8)$

854 to $(\eta_1 = 1, Fr = 0)$ with smaller values of Ri to its right. (b): The region $Ri < 1/4$ is

855 divided as follows: A, in which no jumps may occur; B, in which jumps of modes 1

856 and 2 are possible; and C, in which only one jump, generally of mode 2, is possible.

857 Flows in B and C are supercritical and the remaining area of the (η_1, Fr) plane is sub-

858 critical. In D, $Ri < 1/4$ and the flow is unstable to KHI but, because waves can

859 propagate upstream (as shown in part (a)), no stationary jumps can occur. (c): The

860 hatched region is where the flow is stable to KHI. Its boundary (thick line) is the

861 stability boundary separating stable flow (to the left) from unstable flow (to the right).

862 Ri is less than $1/4$ in the stable region E at small η_1 to the right of the stability boundary

863 where (as shown in part (b)), hydraulic jumps may occur. The dot-dash line

864 corresponds to $Ri = 1/3$.

865

866 3. Contours of potential temperature, $^{\circ}\text{C}$, and stippled regions in which the rate of

867 dissipation of turbulent kinetic energy per unit mass computed using Thorpe scales

868 exceeds $10^{-7} \text{ W kg}^{-1}$ in a section through the Samoan Passage made while steaming at

869 low speed in tow-yo mode (from Alford et al., 2013, figure 3c). The bottom

870 topography is shown in black. The two sections, 19 – 25 km and 3 – 12 km (i.e., $x =$

871 19 - 25 and 3 - 12), selected for analysis in §§ 3.2 & 3.3, respectively, are marked on

872 the horizontal distance axis.

873

874 4. Profiles of (a): Σ , the potential density, measured in kg m^{-3} , minus 1045.9 kg m^{-3} ,

875 and (b): northward velocity, u , in m s^{-1} in the Samoan Passage at roughly 1 km

876 intervals from about $x = 19$ to $x = 25$. (The actual positions, the mean locations of the

877 two-yo profiles, are $x = 19.1, 20.1, 21, 22, 23.1, 24.1$ and 25.2 .) Successive profiles

878 are displaced to the right by (a) 0.2 kg m^{-3} and (b) 0.15 ms^{-1} . The water depth is

879 indicated by horizontal bars beneath each profile. The position of $u = 0$ for each

880 profile is marked at the top of (b) by vertical arrows. The features marked A to D in

881 (a) are discussed in the text.

882

883 5. Values of η and Fr at numbered kilometer locations in the Samoan Passage (a): $x =$

884 19 – 25 and (b): $x = 3 – 12$. Points to the right of the bold line are supercritical, those

885 to the left subcritical. The uncertainty in observed values of η and Fr is shown by

886 error bars. The dot-dash line corresponds to an interfacial gradient Richardson number

887 of $1/3$.

888

889 6. The model's predictions of (a): the downstream profile parameter, η_2 ; (b): the ratio

890 of flowing layer thickness, $q = h_2/h_1$; and (c): the non-dimensional energy loss, E_n , in

891 the (η_1, Fr) plane. Values of (upstream) η_1 and Fr are indicated at labeled locations, $x =$

892 4.8 and 20 in the Samoan Passage where, according to the model, the flow becomes

893 supercritical.

894

895 7. Contours of potential density at intervals of $5 \times 10^{-3} \text{ kg m}^{-3}$ between $x = 19.1$ and $x =$

896 24.1 and depths ranging from 4400 m to 4900 m in the Samoan Passage. The mean

897 horizontal locations of vertical profiles made by the tow-yo are indicated by dots on

898 the x -axis. The flow becomes supercritical at $x \approx 20$. The approximate position of the

899 mixing region associated with the hydraulic jump is indicated by the oval shaped
 900 curve. The step-like structure of the unsmoothed contours sloping downwards from x
 901 $= 19.1$, $z = 4680$ m is probably unreal, a consequence of interpolation by the computer
 902 package used to construct the contours as a narrow density interface moves
 903 downwards as x increases.
 904

905 8. Contours of potential density at intervals of $5 \times 10^{-3} \text{ kg m}^{-3}$ through the hydraulic
 906 jump between $x = 4$ and $x = 7$ below 4300 m depth in the Samoan Passage. The mean
 907 horizontal locations of vertical profiles made by the tow-yo and the depth of the
 908 seabed are indicated by the dots. Tow-yo profiles extend only to about 40 m from the
 909 seabed so no data are available closer to the seabed. The flow becomes supercritical at
 910 $x \approx 4.8$. The approximate position of the oval shaped mixing region associated with
 911 the hydraulic jump is outlined.
 912

913 9. The critical curves of figure 2 translated to the (η_l, Fr_P) plane. Regions A – E
 914 correspond to those in figure 2, b&c. The thick line represents the lowest values of
 915 Fr_P at which a hydraulic transition can occur for given η_l . In (a) points are taken from
 916 Peters & Johns (2005) in the two channels, NC and SC, of the Red Sea Outflow. (b)
 917 shows points taken from Gasser et al. (2011) and Nash et al. (2012) at stations UTS
 918 and DTS in the Mediterranean Outflow. The dot-dash line corresponds to an
 919 interfacial gradient Richardson number of $1/3$.
 920

921 10. Contours of potential density at intervals of $5 \times 10^{-3} \text{ kg m}^{-3}$ through the hydraulic
 922 jump between $x = 19.4$ and $x = 24.7$ and in depths ranging from 4400 m to 4900 m in
 923 the Samoan Passage obtained approximately 2 years later than those of the jump
 924 shown in figure 7. The mean horizontal locations of vertical profiles made by the tow-
 925 yo are indicated by dots on the x -axis. The approximate position of the mixing region
 926 associated with the hydraulic jump is indicated by the oval shaped curve.

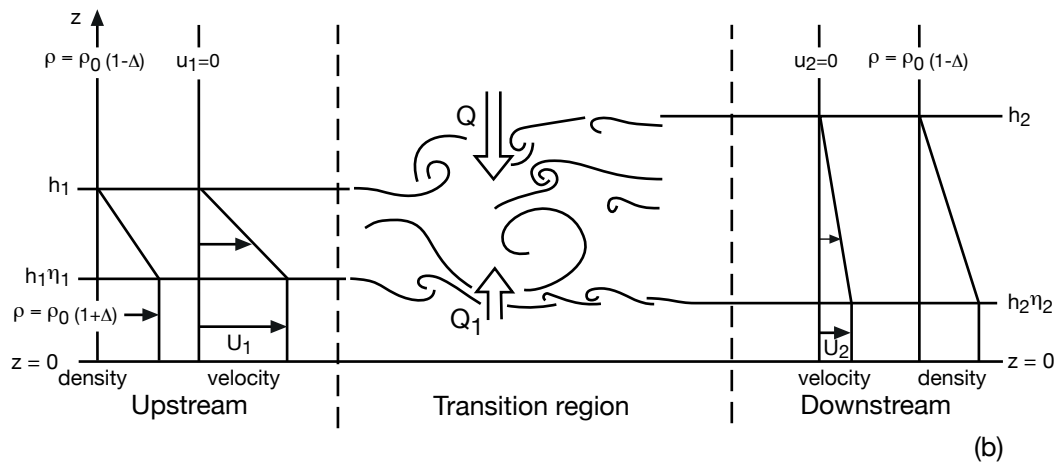
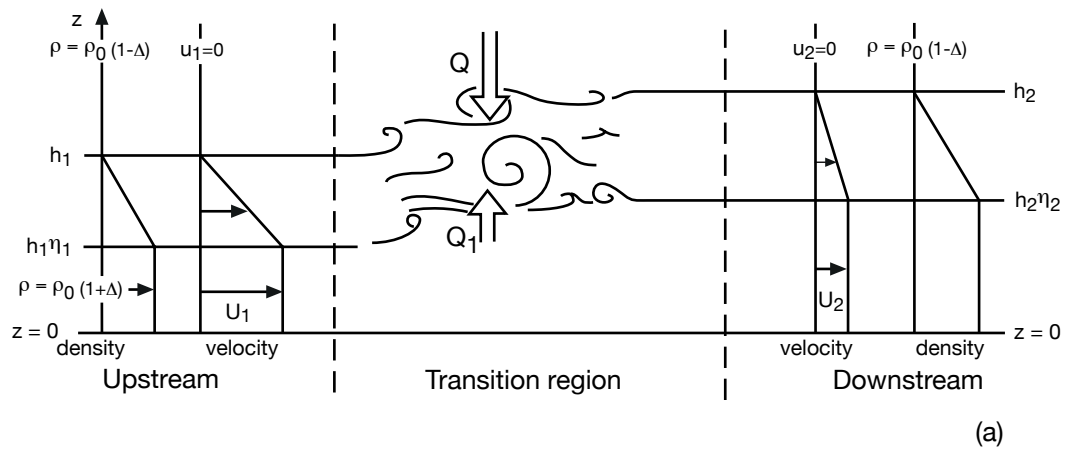


Figure 1.

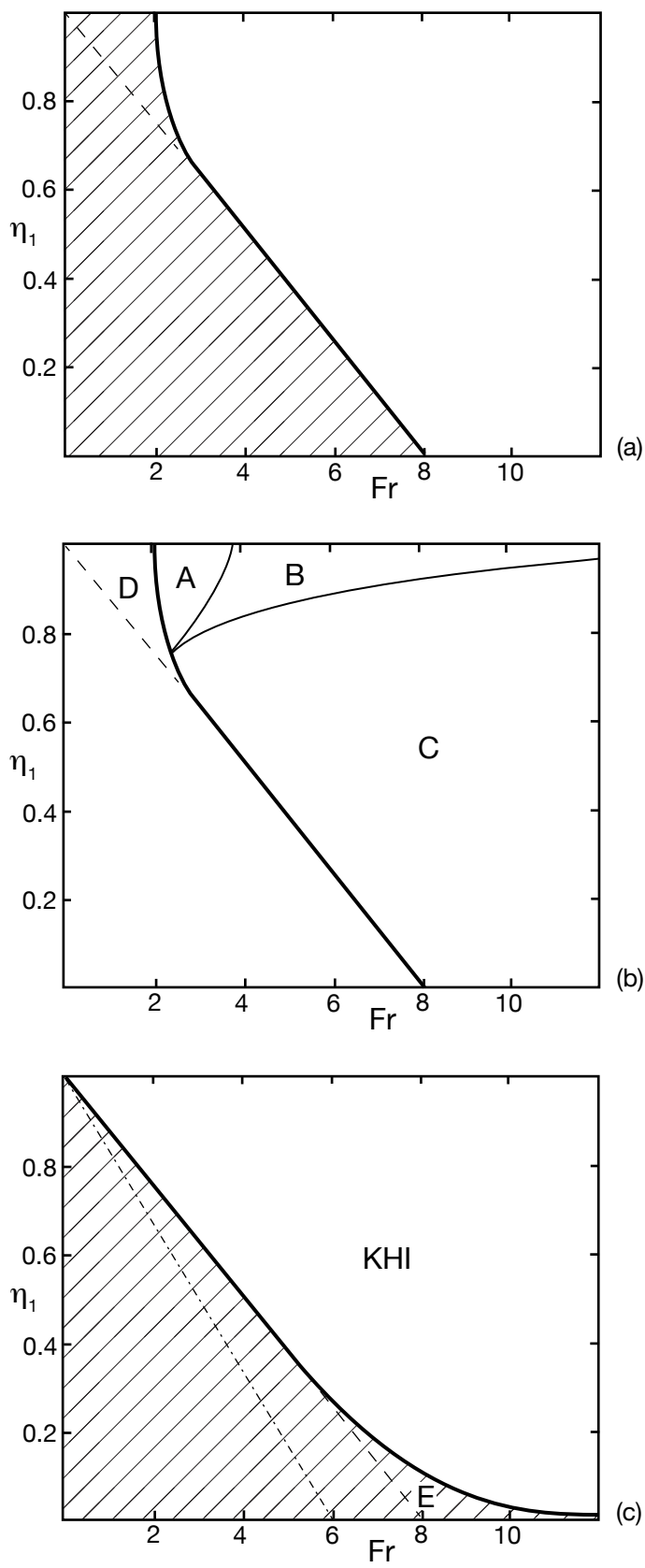


Figure 2

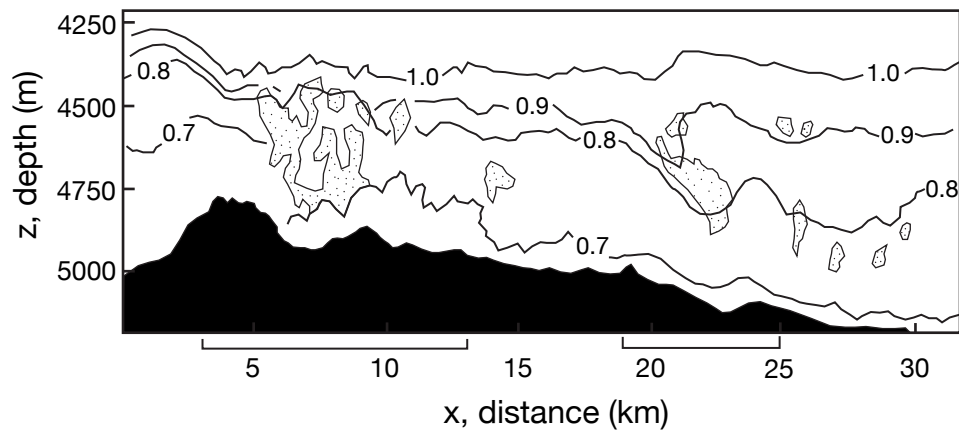


Figure 3

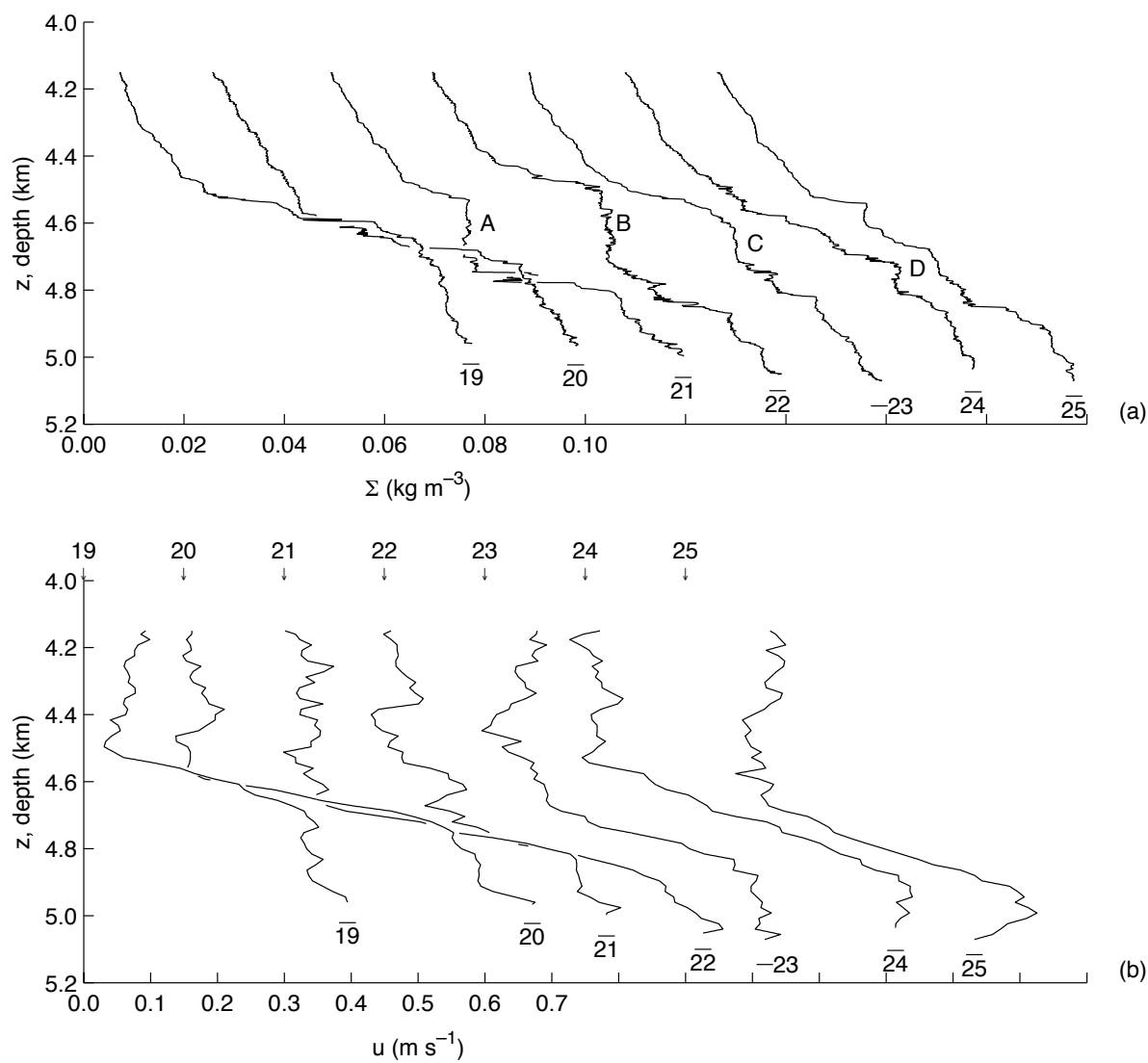


Figure 4

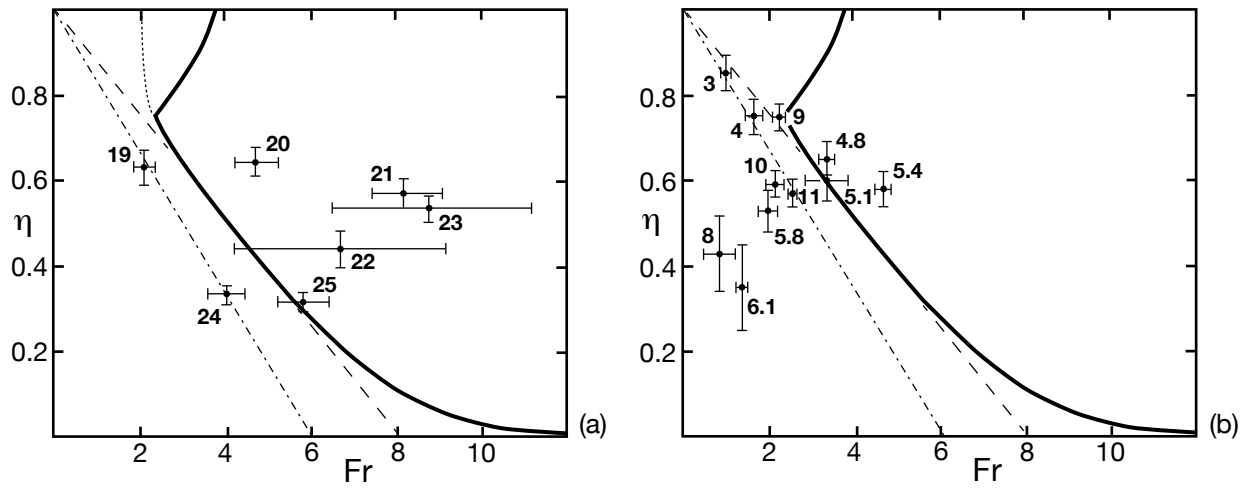


Figure 5

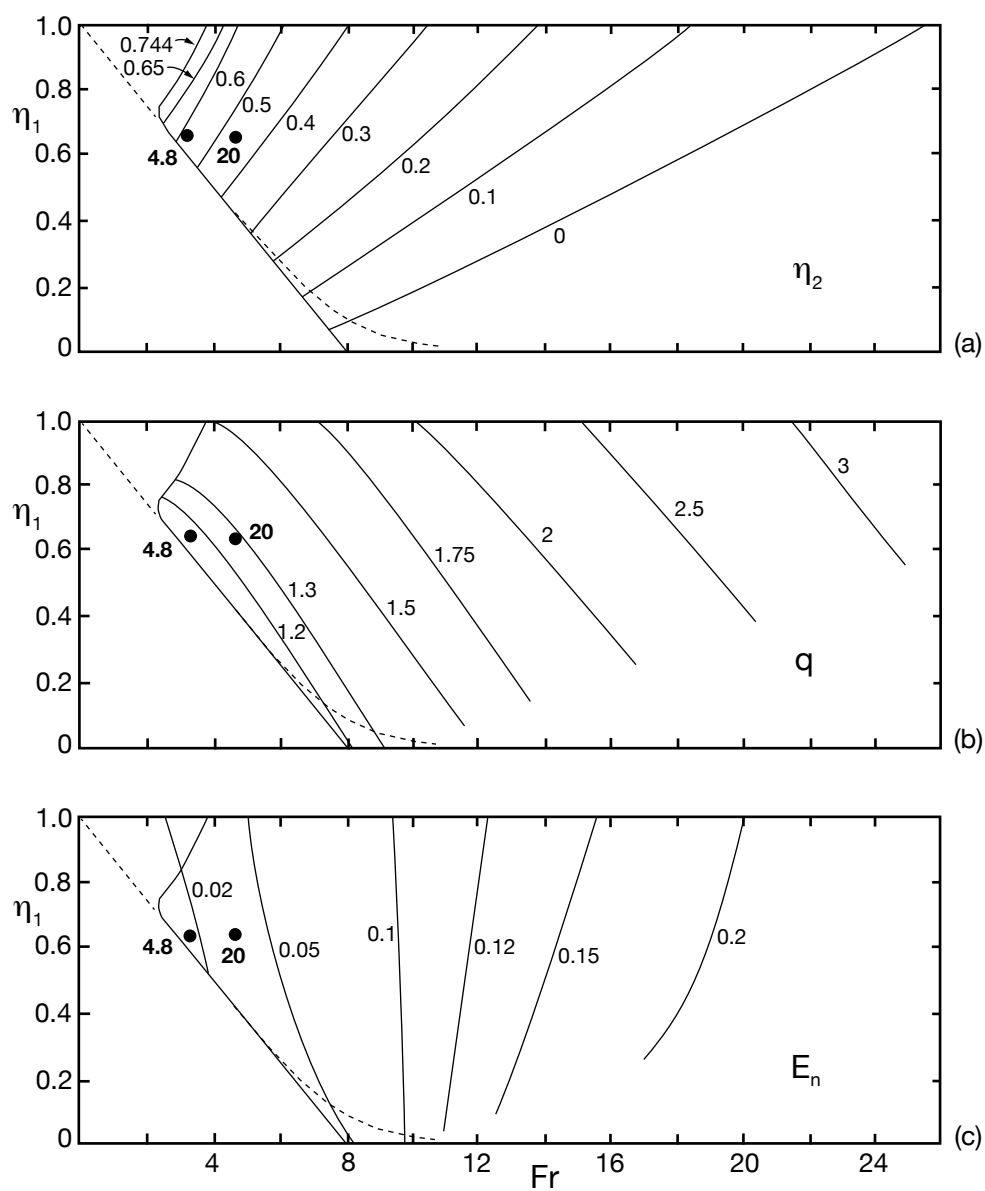


Figure 6

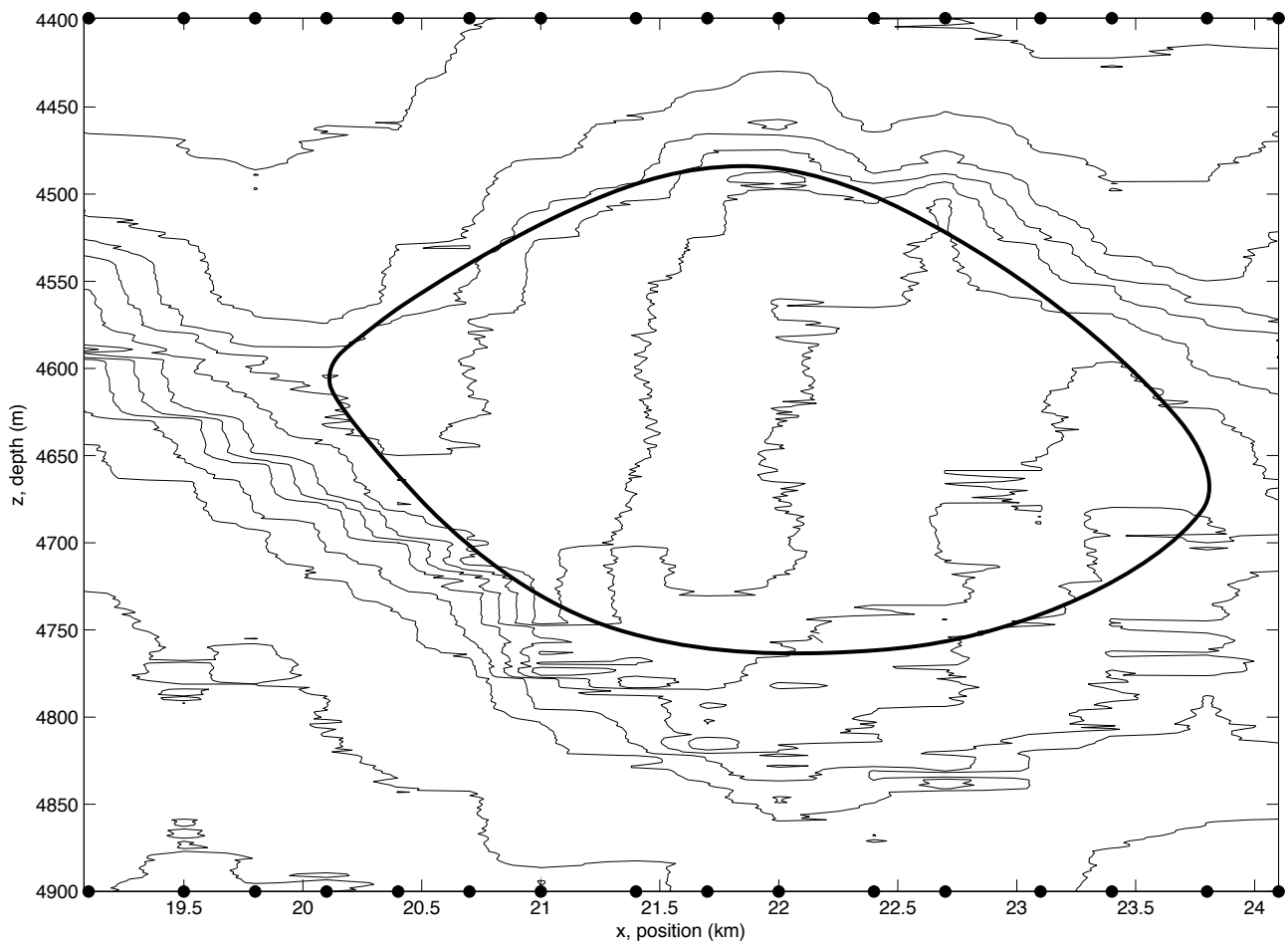


Figure 7

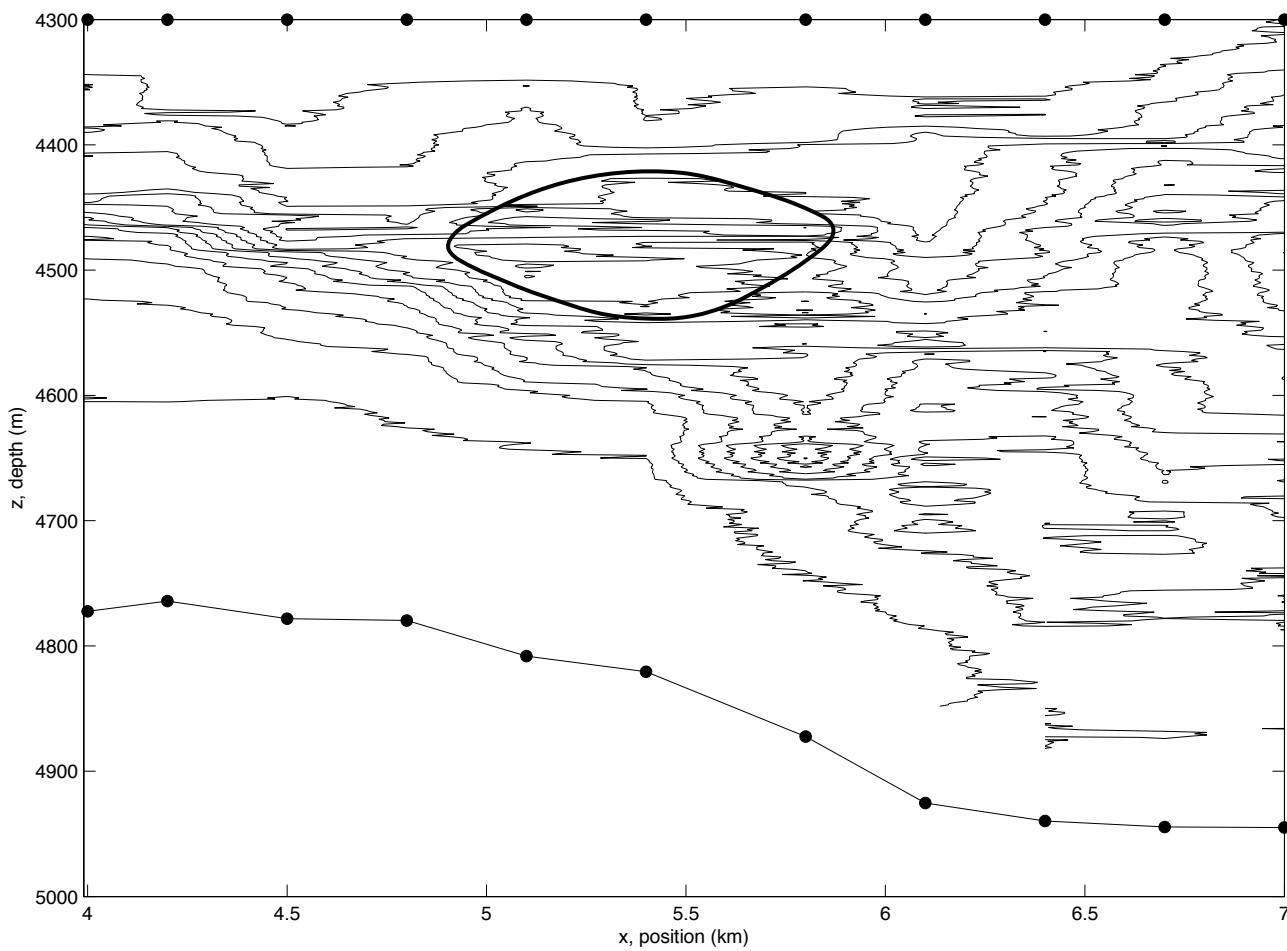


Figure 8

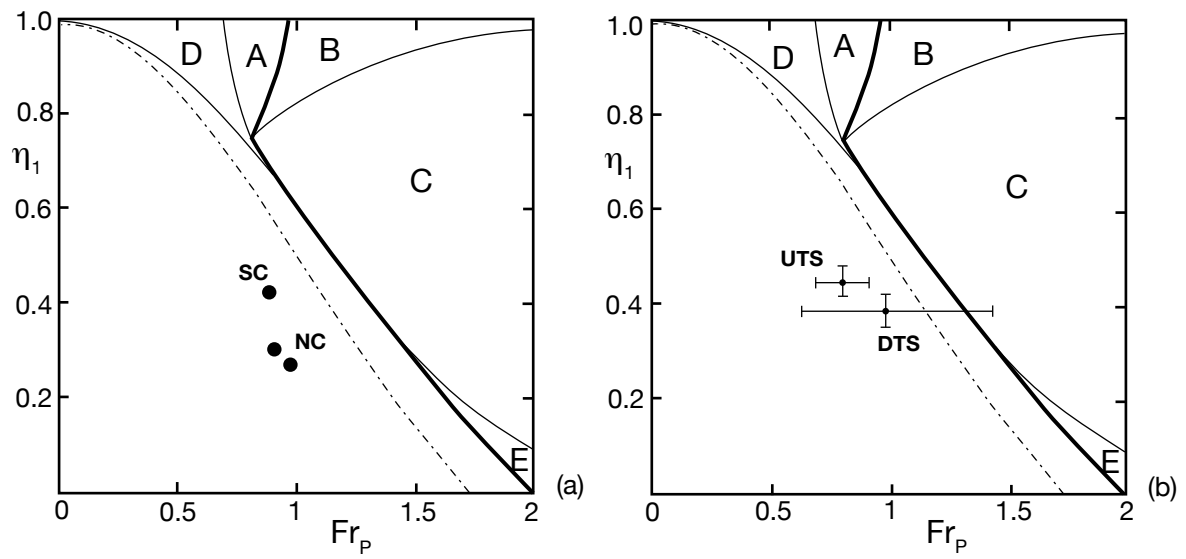


Figure 9

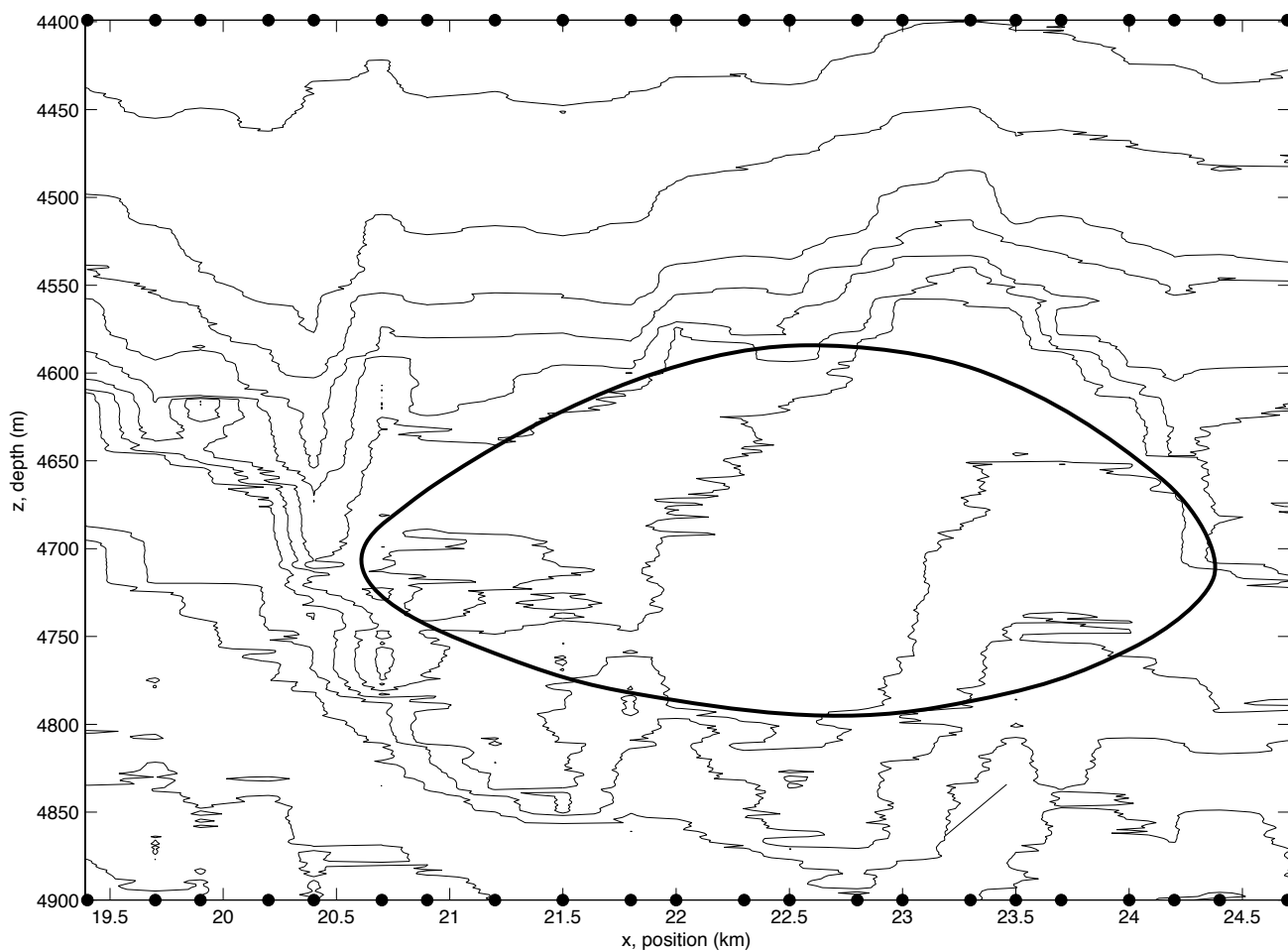


Figure 10